International Journal of
Geo-Information

Article

Comparison of GNSS-, TLS- and Different Altitude UAV-Generated Datasets on the Basis of Spatial Differences

Huseyin Yurtseven

Department of Surveying and Cadastre, Faculty of Forestry, Istanbul University—Cerrahpasa, Istanbul 34473, Turkey; huseyiny@istanbul.edu.tr; Tel.: +90-212-338-2400

Received: 8 March 2019; Accepted: 1 April 2019; Published: 3 April 2019

Abstract: In this study, different in-situ and close-range sensing surveying techniques were compared based on the spatial differences of the resultant datasets. In this context, the DJI Phantom 3 Advanced and Trimble UX5 Unmanned Aerial Vehicle (UAV) platforms, Zoller + Fröhlich 5010C phase comparison for continuous wave-based Terrestrial Laser Scanning (TLS) system and Network Real Time Kinematic (NRTK) Global Navigation Satellite System (GNSS) receiver were used to obtain the horizontal and vertical information about the study area. All data were collected in a gently (mean slope angle 4%) inclined, flat vegetation-free, bare-earth valley bottom near Istanbul, Turkey (the size is approximately 0.7 ha). UAV data acquisitions were performed at 25-, 50-, 120-m (with DJI Phantom 3 Advanced) and 350-m (with Trimble UX5) flight altitudes (above ground level, AGL). The imagery was processed with the state-of-the-art SfM (Structure-from-Motion) photogrammetry software. The ortho-mosaics and digital elevation models were generated from UAV-based photogrammetric and TLS-based data. GNSS- and TLS-based data were used as reference to calculate the accuracy of the UAV-based geodata. The UAV-results were assessed in 1D (points), 2D (areas) and 3D (volumes) based on the horizontal (X- and Y-directions) and vertical (Z-direction) differences. Various error measures, including the RMSE (Root Mean Square Error), ME (Mean Error) or MAE (Mean Average Error), and simple descriptive statistics were used to calculate the residuals. The comparison of the results is simplified by applying a normalization procedure commonly used in multi-criteria-decision-making analysis or visualizing offset. According to the results, low-altitude (25 and 50 m AGL) flights feature higher accuracy in the horizontal dimension (e.g., mean errors of 0.085 and 0.064 m, respectively) but lower accuracy in the Z-dimension (e.g., false positive volumes of 2402 and 1160 m^3, respectively) compared to the higher-altitude flights (i.e., 120 and 350 m AGL). The accuracy difference with regard to the observed terrain heights are particularly striking, depending on the compared error measure, up to a factor of 40 (i.e., false positive values for 120 vs. 50 m AGL). This error is attributed to the "doming-effect"—a broad-scale systematic deformation of the reconstructed terrain surface, which is commonly known in SfM photogrammetry and results from inaccuracies in modeling the radial distortion of the camera lens. Within the scope of the study, the "doming-effect" was modeled as a functional surface by using the spatial differences and the results were indicated that the "doming-effect" increases inversely proportional to the flight altitude.

Keywords: accuracy assessment; terrestrial laser scanning; unmanned aerial vehicle; digital surface model; "doming effect"; structure from motion

1. Introduction

Considering recent developments, different equipment and methods are used in the generation of information related to the surface of the ground and objects on it. The spatial data to be used in the generation of the spatial information can be acquired with two different approaches. The first is to collect the data using ground-based surveying techniques. At this stage, many different equipment can be used, such as Global Navigation Satellite System (GNSS) receivers, total station (TS), terrestrial laser scanner (TLS), etc. [1]. The other approach is to collect the spatial data using remote sensing techniques such as photogrammetry, radar-based and laser-based techniques [2,3]. Although the ground-based surveying techniques are more accurate than the remote sensing techniques, the data acquisition can be time-consuming when the applications require high-resolution information [4]. In the last decade, unmanned aerial vehicle (UAV)-based photogrammetric and laser-based surveying systems have become popular in recent years due to their advantages. In obtaining ultra-high-resolution (UHR) data in small areas, TLSs and UAVs can be operated at optimal costs with high accuracies [5]. However, many factors affect the accuracy of the datasets to be produced. In this context, the TLS-derived dataset accuracy is mostly affected by user-based errors, which are usually caused by the creation of a scanning pattern in the field without considering the TLS specifications or the topography. Equipment-based errors are related to the technical specifications of the TLS, which are provided by the system manufacturers often in an incomparable manner [6,7]. Other important error sources are the surface reflectance or reflectivity of the scanned object and the Ground Control Point (GCP) coordinate accuracy in georeferencing.

The factors that affect the accuracy of UAV-based photogrammetric data can be classified into six categories. The first category is related to GCP features such as the distribution, coordinate accuracy and number of GCPs [8]. The second category is related to on-UAV data collection systems and their features. The camera [9,10], Inertial Measurement Unit (IMU) [11], GNSS receiver features [12] and IMU-GNSS-camera timing synchronization and locational calibration on the UAV platform [13] directly affect the accuracy of the photogrammetric data. The flight and data acquisition parameters can be grouped into another category, such as the flight path pattern (parallel or cross) [14], flight altitude [15,16], number of photos, overlap ratio [17], and acquiring nadir or off-nadir (oblique) imagery [18]. For the study area, the topographic characteristics [19,20], area size, lighting conditions and color contrast of ground objects are also important variables. UAV platform characteristics such as the flight principle (fixed wing, multicopter, etc.) and gimbal precision (if gimbal is used) affect the vibration or speed. The speed and vibration can cause a blurring effect on images. The last category is related to photogrammetric software algorithms. The use of approaches such as Structure from Motion (SfM), Multi-View Stereo (MVS), and conventional affects the accuracy of the resulting datasets [21–24].

Nowadays, the use of SfM-based photogrammetry is preferred for topographical modeling and ortho-data generation using images acquired with UAVs and low-cost or not-metric cameras [25–30]. After recent developments in computer vision technology, SfM has gained popularity as an inexpensive solution compared to traditional photogrammetry to extract the 3D structure of a scene from multiple overlapping photographs [31,32]. Many commercial and open-source software packages use SfM algorithms. Although UAV-SfM-based data achieve UHR details, they can also have systematic errors such as "doming", which restrict their wider use [33].

The "doming effect" is a broad-scale systematic deformation of the SfM-based reconstructed terrain surface and is related to exclusively nadir imagery collection, the using of near-parallel flight paths or incorrect specification of the camera intrinsic parameters [21,33]. Taking the off-nadir imagery and designing a distributed network of GCPs can help to mitigate the "doming effect" [33–36]. Wackrow and Chandler [37] demonstrated that defining the relationship between the "domes" and the lens model could minimize this systematic error. Magri and Toldo [38] used an automatic ground detection method to capture the doming deformation as a paraboloid plane and used the estimated paraboloid as a parameter to correct the scene geometry. However, the "doming effect" is only mitigated and not completely removed using these approaches.

This study investigated the effects of different altitudes, platforms and camera combinations on the data accuracy and "doming effect" by keeping other error sources constant. For this purpose, an experimental environment was created. A UAV-SfM-based photogrammetric point cloud (PC) and ortho-mosaic datasets were generated using one low-cost (DJI Phantom 3 Advanced) and one mapping purpose (Trimble UX5) UAV system at four different flight altitudes. The reference datasets were collected with two state-of-the-art surveying instruments (TLS and GNSS) to serve the accuracy assessment analysis. Accuracy assessments were performed in all three dimensions based on the spatial differences. Various error metrics were calculated for the point-based horizontal (X and Y) and vertical (Z) coordinate and the surface model-based areal and volumetric differences. All difference metrics were normalized to percentage scores, so the comparison could be performed in a single denominator. According to the obtained comparison results, the "doming effect" was modeled and discussed in different perspectives. These results are considered a guide for the UAV community in selecting the appropriate method to generate the UAV-SfM based UHR datasets.

2. Materials and Methods

Within the scope of the study, a special workflow was established (Figure 1), and the study area was prepared according to the study goals.

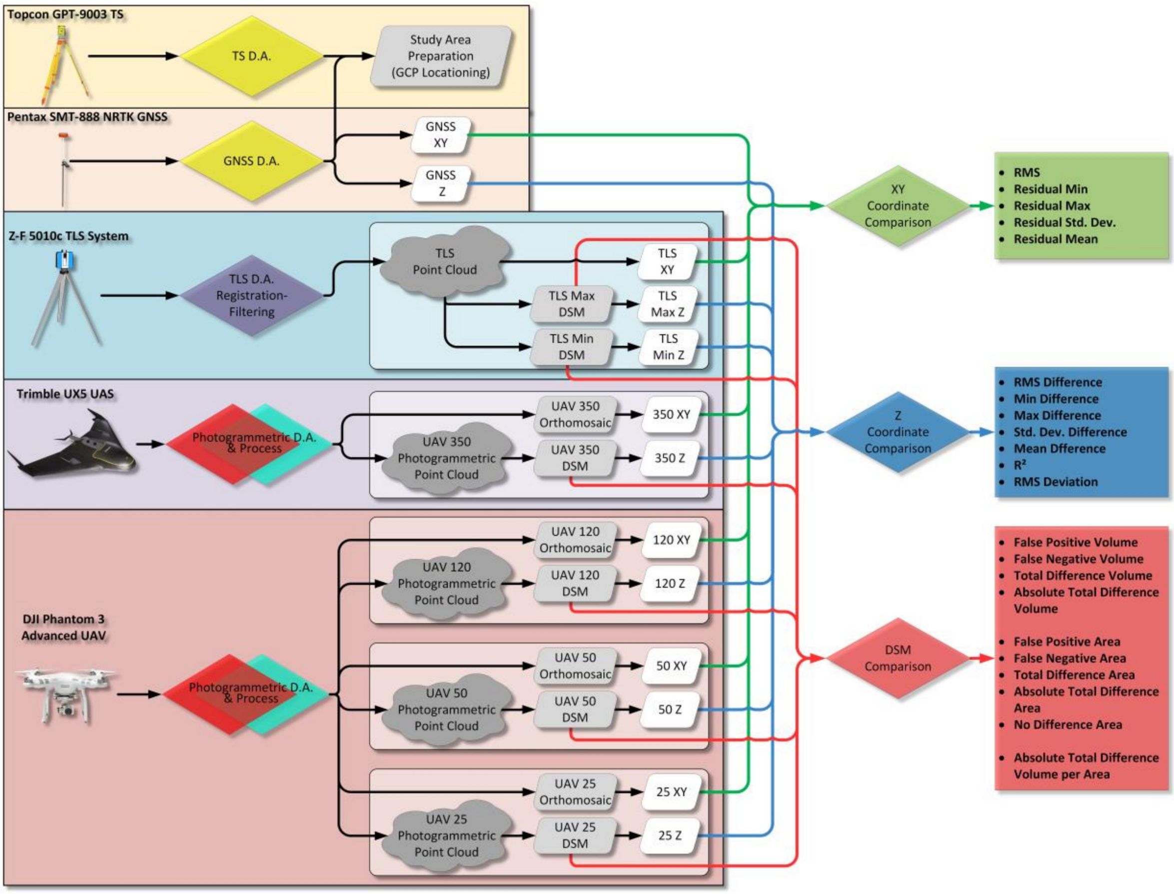

Figure 1. General workflow.

2.1. Study Area

The study area is located in the northern part of Istanbul University—Cerrahpasa Education Research and Practice Forest near Sariyer, Istanbul (41°10′20″ N, 28°59′56″ E). The study area dimension is approximately 40 m wide and 200 m long, which covers an area of 6566.6 m^2; the slope is stable and approximately 4% (Figure 2). The most important factor in the selection of the study area is the presence of a vegetation-free bare earth. Some problems may arise in the modeling of the vegetation top surface with TLS. Hence, the study was performed in a bare earth area, where the data could be more objectively assessed.

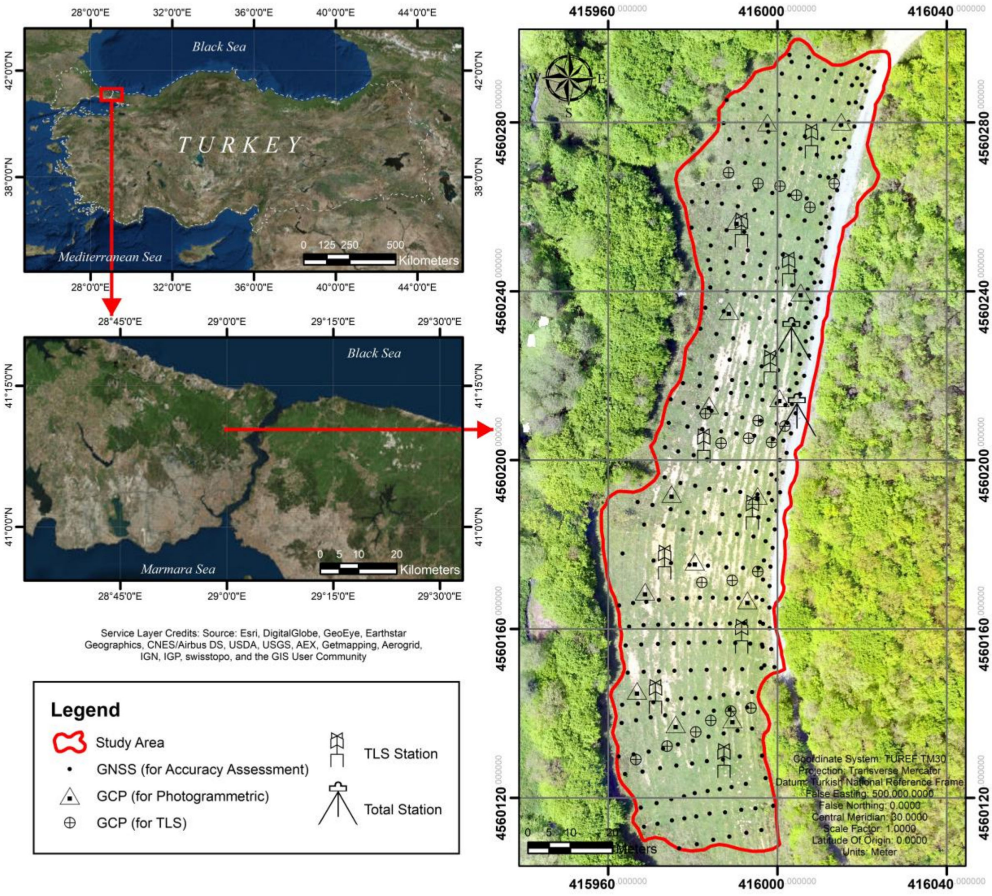

Service Layer Credits: Source: Esri, DigitalGlobe, GeoEye, Earthstar Geographics, CNES/Airbus DS, USDA, USGS, AEX, Getmapping, Aerogrid, IGN, IGP, swisstopo, and the GIS User Community

Figure 2. Study area.

2.2. Data Acquisitions

In this study, five different surveying systems were used for the data acquisition. To ensure the spatial alignment of the data obtained from different data sources (with GCPs) for the accuracy analysis (as reference points), in total, 377 points were established in the study area by using National Continuously Operating Reference Stations (CORS)-based Network Real-Time Kinematic (NRTK) GNSS (Pentax SMT-888) receiver. Two of these points were used as stationary points for the TS-based surveying. Fifteen specially designed GCP plates were distributed across the study area as photogrammetric GCPs. In this context, two types of GCP plates were used: 1-m GCP plates were used in the 350-m flight altitude (AGL) data acquisitions, and 0.3-m GCP plates were used in the 25-, 50- and 120-m flight altitude (AGL) data acquisitions. TS stationary points and photogrammetric GCPs were not used as reference in the accuracy analyses. Then, 35 of the remaining 360 points were marked with spray paint to the ground and used as the reference point (RP) to determine the X- and Y-coordinate accuracy. All 360 points were used as RPs to determine the Z-coordinate accuracy (Figure 2). All point coordinates were surveyed in the Turkish National Reference Frame (TUREF) Transverse Mercator (TM) 30 (Central Meridian) (EPSG: 5254) coordinate system. Each coordinate measurement was performed with a 10-s session, so that the GNSS field works were completed in 3 h 6 min in total.

The TLS-based data collection was performed to generate the surface model, which was accepted as a reference. The Zoller+Fröhlich 5010c phase-based (phase comparison for continuous wave) TLS System was used to obtain terrestrial PC data with 0.018° angular resolution. The TLS system can scan up to 187 m range with 360° horizontal and 320° vertical angle from each scan station. Between two scan stations, the approximate horizontal distance was 20 m, and TLS was installed at approximately 2 m height at each scan station. Six portable targets were used as the GCP to register the PC data of each scan station to the other and georeference to the project coordinate system (TUREF TM30, EPSG: 5254). In total, 21 TLS GCPs were established, and the coordinate acquisitions were simultaneously performed with TS to the TLS process (Figure 3). With this data acquisition pattern, the TLS field works were accomplished with 10 TLS scan stations in 2 h 35 min.

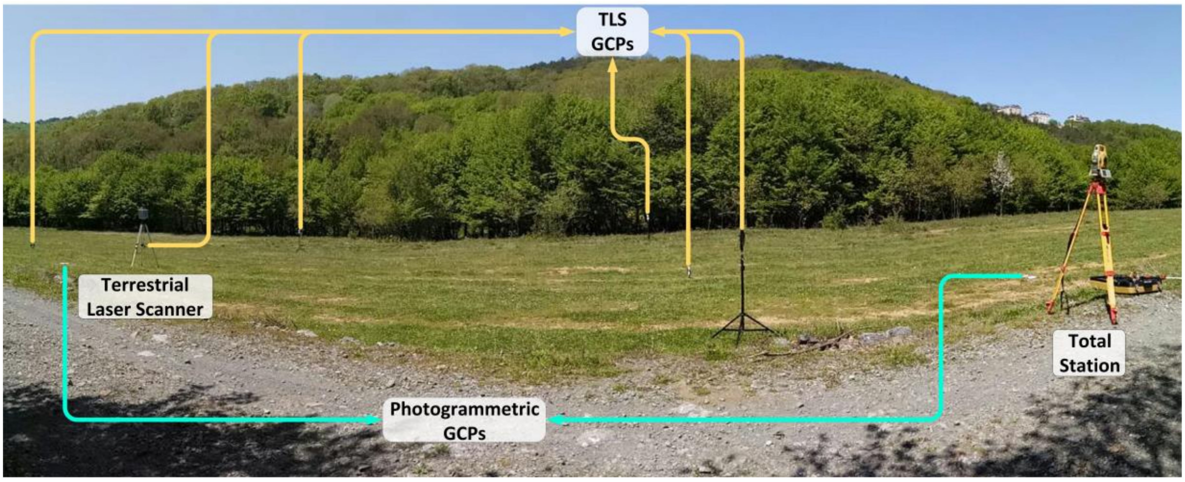

Figure 3. TLS and TS data acquisition.

Photogrammetric data acquisitions were performed with the Trimble UX5 UAS and DJI Phantom 3 Advanced UAV platforms (Table 1).

Table 1. UAV platform specifications.

Features	Trimble UX5	DJI Phantom 3 Advanced
Platform Type	Fixed Wing	Multicopter
Purpose	Mapping	Hobby, photography, videography
Takeoff-Landing	Takeoff: Catapult launch Landing: Belly (Min. 50 m × 30 m open area for landing)	Vertical takeoff and landing
Cruise Altitude (from Takeoff Location) (Min—Max)	Min.: 75 m Max.: 750 m	(Mapping purpose autonomous flight) Min.: 10 m Max.: 500 m
Endurance	50 min.	23 min.
Max Operation Distance	5000 m	3500 m
Cruise speed	80 km/h	Min.: 0 km/h Max.: 57 km/h
Camera Properties	Fixed RGB or NIRRG Sony Nex5T mirrorless APSC Res.: 4912 × 3264 pixels (16MP) FOV: 84° Focal Lenght: 15.517 mm Pixel Length: 4.75 micron	RGB with Gimbal Res.: 4000 × 3000 pixels (12MP) FOV: 94° Focal Lenght: 3.61 mm Pixel Length: 1.56 micron
Positional Data Recording	L1 GNSS (X, Y, Z Coor.) IMU (Yaw, Pitch, Roll Angles)	L1 GNSS (X, Y, Z Coor.)
Cost (Approximately in Turkey)	65,000 USD	1000 USD

Photogrammetric data acquisitions were performed at four different flight altitudes (25, 50, 120 and 350 m AGL). The 25-, 50- and 120-m AGL data acquisitions were performed with the DJI Phantom 3 Advanced UAV, and the 350-m AGL data acquisition was performed with the Trimble UX5 UAS platform (Table 2). The study area is located at the bottom of a valley. The fixed-wing Trimble UX5 UAS platform has a large turning radius between flight strips. To obtain flight safety, data acquisitions were not performed under the 350-m AGL flight altitude with the Trimble UX5 UAS platform. The minimum AGL flight altitude of 25 m was decided by considering the maximum tree height in the study area. The AGL altitudes of 25 and 50 m offer 1- and 2-cm ground sampling distances (GSD), respectively. The AGL altitude of 120 m (~400 feet) is the maximum altitude allowed for civil flights as specified in the UAV regulations of most countries [39–43]. Since the 120-m flight altitude (AGL) can be accepted as an international maximum standard for UAV operations, it was preferred as an alternate flight altitude.

Table 2. Flight parameters.

Flight Altitude	UAV Platform	Overlap Ratios (% Forward—% Side)	Number of Photos	Flight Duration	Total 3D Model Area (m^2)
25 m	DJI Phantom 3 Advanced	95–95%	483	21 min	19,610.60
50 m	DJI Phantom 3 Advanced	95–95%	344	15 min	33,898.84
120 m	DJI Phantom 3 Advanced	95–95%	94	5 min	81,870.75
350 m	Trimble UX5	80–80%	42	6 min	371,640.92

2.3. Data-Processing and Accuracy Assessment Procedures

The photogrammetric processes were performed with the Agisoft PhotoScan Professional Edition V1.2.2 software (http://www.agisoft.ru), which uses SfM-based techniques. Initially, the cameras in two UAV systems were calibrated with a set of checkerboard images. The camera calibration parameters, image coordinates and image orientation (yaw, pitch, roll) parameters (for Trimble UX5 imagery) were defined for each project. Then, the tie points were determined for each image pair, and a georeferenced image block was generated by using 15 GCPs in addition to the aforementioned parameters. Finally, photogrammetric PCs and ortho-mosaics were generated from the image blocks.

All TLS-based raw scans were registered and georeferenced using the Z+F LaserControl V8.6.0 software in the accordance with 21 TLS GCP coordinates. After the geo-referencing, the noise data were filtered with the "Range Filter" to remove the points that should not be in the range of 0.5–1 m from the TLS location. Then, the laser-based PC was archived with the intensity information for analysis.

After the data acquisitions and pre-processing, three different data types were prepared for analysis: PCs, ortho-imagery and RP locations on the generated datasets. First, PC data obtained from four different sources were clipped by the boundary data of the study area for the objective evaluation. After clipping, all PC data were transformed to raster-based DSM with the gridding procedure. Gridding is the most efficient method to eliminate the irregularly spaced point-to-point distances [44–47]. The choice of the optimal grid resolution is an ongoing research topic and related to many different factors such as the point density, spatial accuracy of points, size of the area, processing power of the computer, geometry of the point patterns, complexity of the terrain, cartographic standards, and gridding or interpolation technique requirements [48,49]. In the gridding procedure, various interpolation techniques have been studied by researchers, and each technique has its own advantages depending on the characteristics of the datasets [50–60]. Interpolation is generally used to obtain the values at unsampled locations [61] based on the geographic principle of "everything is related to everything else, but near things are more related than distant things" [62]. In studies using UAV or TLS systems, the data resolutions or point densities are very high especially in the TLS dataset, which implies that there is also no unsampled location in the research area. Therefore, the use of an interpolation procedure was considered superfluous to grid all datasets. However, in these datasets, there may be areas with low data densities due to different error sources such as noise or image matching conflicts. This situation causes irregularly spaced data densities. At this point, to objectively evaluate the datasets, the inverse distance weighted (IDW) interpolation with the binning approach was used for gridding. Binning techniques provide a simple and natural method to handle large amounts of data [63,64]. The binning approach lays a regular grid over the PC dataset, and the minimum, maximum or average of point elevations in each bin grid is accepted as a grid value.

The bin size or resolution of the grid structure (r) was determined from the point density (d) of the area of interest (points per m^2) using Equation (1).

$$r = \frac{1}{\sqrt{d}} \tag{1}$$

This equation is basically based on the principle that there should be one point in each grid cell. However, due to irregular point spacing, some grids do not have any point, or some of them have more than one points. If a grid does not have any point in it, the IDW interpolation is used to estimate the grid value from the neighbor grid points. Contrarily, if a grid has more than one point in it, the minimum, maximum or average of point elevations can be used as a grid value.

Photogrammetric and laser-based PCs have different data characteristics. The 3D model obtained from photogrammetric processes is related to the upper surface of the object or the ground. Thus, the transformation of the photogrammetric PC data to raster the surface model was performed using the average binning combined IDW approach. Meanwhile, the 3D model generated by the laser scanning process, which is an active remote sensing tool, is formed by laser beams, which enables the modeling of every surface that can be reached by laser beams. For example, the upper surface of the vegetation and the area under the vegetation surfaces can be modeled by the laser beams that pass through the gaps. In the gridding stage of the TLS based PC data, two different raster datasets were generated using the minimum and maximum binning combined IDW approach. These two datasets actually represent the bare earth surface model (digital elevation model, DEM) and the surface model (digital surface model, DSM).

After obtaining the surface models, the accuracy assessment procedures were performed. In this stage, the point and surface model-based differences were investigated. The point-based assessments were performed by separately evaluating the horizontal (X and Y) and vertical (Z) coordinate differences, surface-based evaluations were performed by evaluating the areal and volumetric differences of the DSMs. Although TLS- and GNSS-based data were used as a reference, the cross evaluation was performed to evaluate the differences among all data.

To obtain the horizontal (X and Y) coordinate accuracy, six datasets were compared by using the residuals and root mean square errors (RMSE) of 35 RPs. The RP locations were interpreted from each photogrammetric ortho-mosaic (25-, 50-, 120- and 350-m AGL) and the TLS-based data. Since the PC data did not contain color information, RP locations were interpreted from the ortho-model obtained from the PC intensity information (also called reflectance values).

$$\mathrm{RMSE}_{(X,Y)} = \sqrt{\frac{1}{n}\sum_{i=1}^{n}\left[\left(x_{\mathrm{Eva}(i)} - x_{\mathrm{Ref}(i)}\right)^2 + \left(y_{\mathrm{Eva}(i)} - y_{\mathrm{Ref}(i)}\right)^2\right]} \tag{2}$$

Vertical (Z) coordinate accuracy analyses were examined over 360 RPs for seven dataset. In this study, six DSM datasets were generated using UAV-based photogrammetric (25-, 50-, 120- and 350-m AGL) and TLS-based (minimum and maximum surface models) techniques. To compute the vertical (Z) coordinate differences among these datasets, the horizontal RP coordinates (collected with CORS-NTRK supported GNSS receiver) were superimposed to the DSM datasets, and the vertical information (Z coordinates) were extracted. Regression analysis was performed to compare the vertical (Z) point coordinates. Then, the vertical residuals were calculated to determine the differences of each dataset. Generally, to determine the accuracy measures to use in the accuracy assessment, distributions of the residuals are tested. However, the normal distribution of the error is a rare case for laser scanning or digital-photogrammetry-derived vertical data due to outliers. Although removing the outliers or mitigating their impact on the population is an approach to achieve a normal distribution, if the outliers are measured as accurately as other members of the population, they should be evaluated with other members of the population. In this context, the normal distribution accuracy measures and distribution-free accuracy measures were used together. The normality of the residual distribution was investigated via quantile–quantile (Q–Q) plots and histograms. The descriptive statistics, mean error (MA), mean absolute error (MAE) and root mean square error (RMSE) of the residuals were calculated and used as the normal distribution accuracy measures. In addition, as suggested by Höhle and Höhle [65], the median and Normalized Median Absolute Deviation (NMAD) of residuals (Δh) were used as distribution free accuracy measures.

$$\mathrm{ME}_{(\mathrm{Z})} = \frac{1}{\mathrm{n}}\sum_{\mathrm{i}=1}^{\mathrm{n}}\left(\mathrm{Z}_{\mathrm{Eva(i)}} - \mathrm{Z}_{\mathrm{Ref(i)}}\right) \tag{3}$$

$$\mathrm{MAE}_{(\mathrm{Z})} = \frac{1}{\mathrm{n}}\sum_{\mathrm{i}=1}^{\mathrm{n}}\left(\left|\mathrm{Z}_{\mathrm{Eva(i)}} - \mathrm{Z}_{\mathrm{Ref(i)}}\right|\right) \tag{4}$$

$$\mathrm{RMSE}_{(\mathrm{Z})} = \sqrt{\frac{1}{\mathrm{n}}\sum_{\mathrm{i}=1}^{\mathrm{n}}\left(\mathrm{Z}_{\mathrm{Eva(i)}} - \mathrm{Z}_{\mathrm{Ref(i)}}\right)^2} \tag{5}$$

$$\mathrm{NMAD} = 1.4826 \cdot \mathrm{median}\left(\Delta \mathrm{h}_{(\mathrm{i})} - \mathrm{median}(\Delta \mathrm{h})\right) \tag{6}$$

The final assessments were made on the DSM datasets by evaluating the areal and volumetric changes. To determine the areal and volumetric differences among the DSMs, the false positive, false negative, no difference, absolute difference zones and absolute difference volume per area were calculated for each pair of datasets. In this context, the false positive defines the zones where the evaluated-reference difference is positive, and the false negative defines the zones where the evaluated-reference difference is negative (Figure 4).

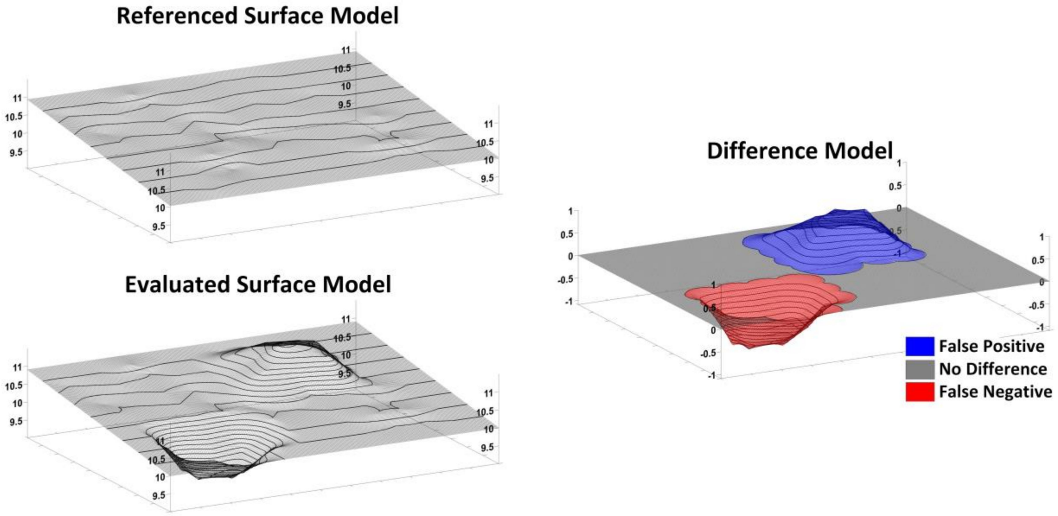

Figure 4. Visual definition of false positive, false negative and no difference areas and volumes.

3. Results

3.1. Data Processing Results

According to the TLS data registration and georeferencing process results, the average, standard and maximum deviations were obtained as 2.6 mm, 1.6 mm and 6.6 mm, respectively. The CORS-NRTK-supported GNSS measurements had near-one centimeter level nominal accuracy. In addition, according to the SfM process results of the 25-, 50-, 120-and 350-m AGL altitude photogrammetric data, total GCP RMSEs were obtained at 0.55, 0.28, 0.04 and 0.01 m, respectively. In this context, the data obtained by TLS and GNSS were proven reliable to use as the reference.

After the dataset generation procedures, all datasets were clipped with the study area border, and the analysis was performed using clipped datasets. DSM resolutions were calculated using Equation (1) according to the point density parameters of each PC dataset. The ultimate datasets properties and visuals are shown on Table 3 and Figure 5.

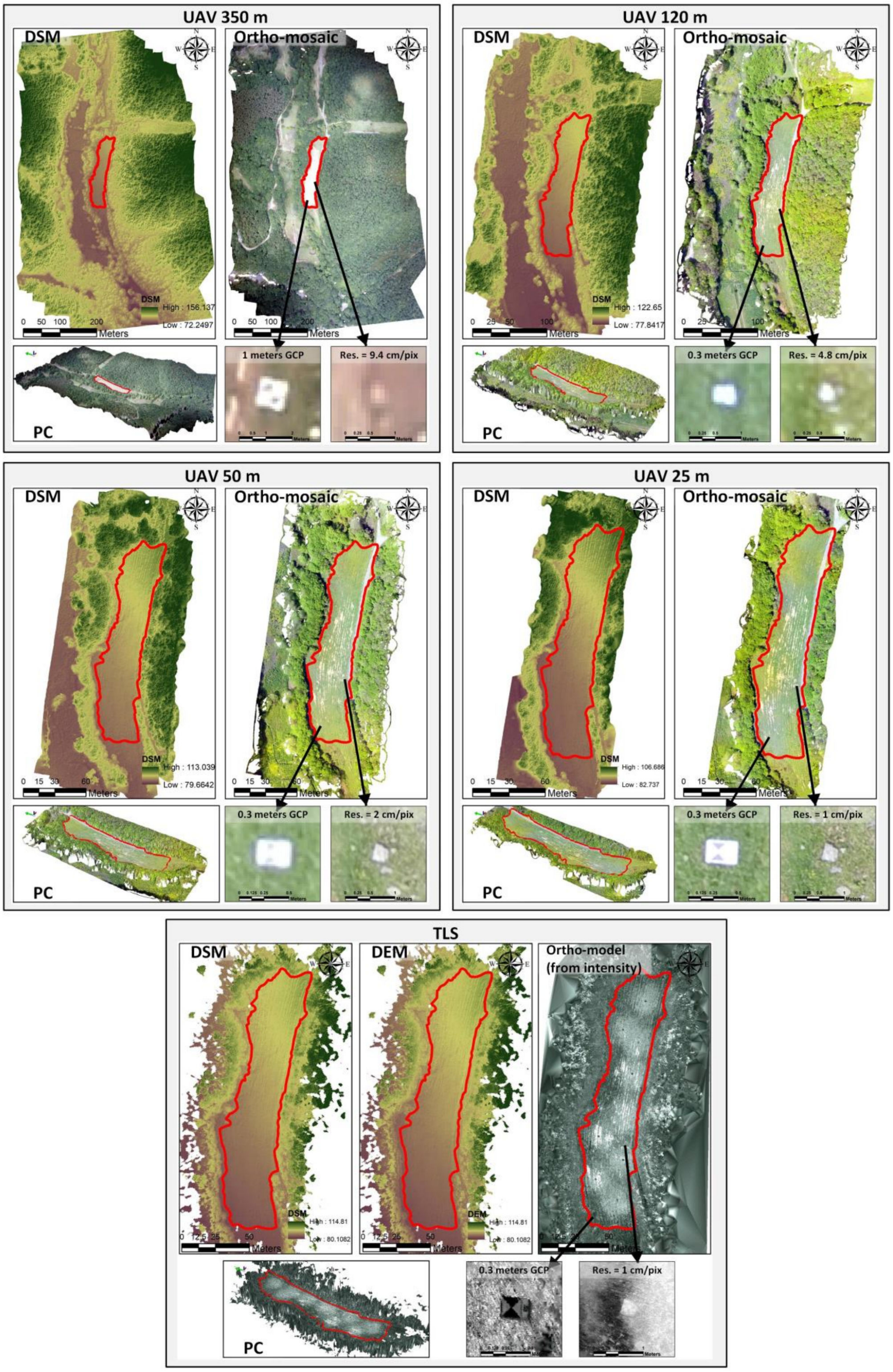

Figure 5. DSM (and DEM for TLS), PC, ortho datasets generated from UAV and TLS -based data.

Table 3. Final dataset properties in study area.

Dataset	Ortho-Mosaic Resolution (m)	Total Point Count inside the Study Area	Point Density (Point/m^2)	Calculated Resolution from Equation (1) (m)	Accepted Resolution for DSM (m)
TLS	***0.006 ****	197,806,322	30,123.096	0.006	***0.010***
UAV 25 m	***0.010***	15,477,265	2356.968	0.021	***0.020***
UAV 50 m	***0.020***	4,669,434	711.089	0.038	***0.040***
UAV 120 m	***0.048***	780,718	118.892	0.092	***0.090***
UAV 350 m	***0.094***	207,076	31.535	0.178	***0.180***

* Intensity data were used to generate ortho-model.

3.2. Accuracy Assessment Results

The accuracy of each dataset type (RP based X-Y, RP based Z and DSM) was analyzed by cross-evaluation of the same-type datasets obtained from different data sources. All obtained difference variables for all datasets in the same accuracy class were compared to each other.

3.2.1. Point-Based Analysis

Point-based vertical and horizontal accuracy assessments were performed separately. To obtain horizontal accuracy, 35 RPs were used. Horizontal accuracies or coordinate differences were examined on six datasets. These datasets were the GNSS-based horizontal (X and Y) RP coordinates, the interpreted horizontal RP coordinates of the TLS intensity-data based ortho-model and 350-, 120-, 50- and 25-m AGL flight altitude ortho-mosaics. In this context, the minimum, maximum, standard deviation and RMS values in each pair of datasets were calculated for the cross-data evaluations (Table 4).

According to the horizontal analysis results, the GNSS-TLS comparison has the best results with 0.1 cm mean and 0.3 cm RMS difference values. These values were interpreted as extraordinary for the 0.6-cm-resolution intensity-based ortho-model and ignored. The comparison results between the GNSS and the ortho-model produced using the data acquired from the flight height of 50 m AGL (GNSS-50) was also remarkable with 6.4 cm mean and 8.5 cm RMS difference values. After these results, the comparison results (mean and RMS) of GNSS-25 (8.5 cm and 11.1 cm), GNSS-120 (9.0 cm and 10.7 cm) and GNSS-350 (10.5 cm and 11.5 cm) were obtained. These results were also supported by TLS measurements. However, the narrowest distribution of difference was achieved by the GNSS-350 comparison with 23.5 cm maximum difference and 4.8 cm standard deviation values.

According to the horizontal coordinate-based analysis results, a simple multi-criteria decision-making analysis was used to find the most reliable dataset. In this context, the mean (Mean Diff.), minimum (Min Diff.), maximum (Max Diff.), RMS difference (RMS Diff.) and standard deviation of horizontal differences (Std. Dev. Diff.) were used, and the results of each type of analysis were normalized to the percentage score according to their maximum and minimum values. The analysis was performed for each dataset type by calculating the same weighted mean of scores. According to the horizontal simple multi-criteria decision-making analysis scores, the GNSS and TLS scores were almost identical. Among the UAV-based data, the 50-m AGL achieved the highest score (Table 5).

Table 4. Horizontal (X,Y) coordinate difference results and frequency-density histograms of residuals.

REFERENCED		EVALUATED					
		GNSS XY	**TLS XY**	**350 XY**	**120 XY**	**50 XY**	**25 XY**
GNSS XY	**Residual (m)**	**Min**	0.000	***0.021***	***0.009***	***0.009***	***0.010***
		Max	0.009	***0.235***	***0.323***	***0.259***	***0.281***
		StdDev	0.002	***0.048***	***0.058***	***0.057***	***0.071***
		Mean	0.001	***0.105***	***0.090***	***0.064***	***0.085***
		RMS (m)	0.003	***0.115***	***0.107***	***0.085***	***0.111***
TLS XY	**Residual (m)**	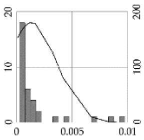	**Min**	***0.022***	***0.009***	***0.009***	***0.010***
			Max	***0.236***	***0.322***	***0.258***	***0.280***
			StdDev	***0.048***	***0.058***	***0.056***	***0.071***
			Mean	***0.105***	***0.090***	***0.064***	***0.084***
			RMS (m)	***0.115***	***0.107***	***0.085***	***0.110***
350 XY	**Residual (m)**	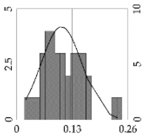	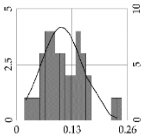	**Min**	0.013	0.013	0.025
				Max	0.261	0.454	0.506
				StdDev	0.053	0.083	0.108
				Mean	0.124	0.128	0.150
				RMS (m)	0.135	0.152	0.185
120 XY	**Residual (m)**	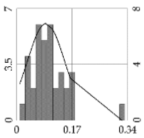	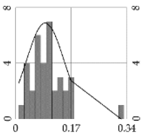	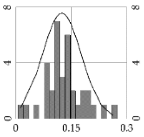	**Min**	0.010	0.004
					Max	0.211	0.251
					StdDev	0.040	0.068
					Mean	0.079	0.105
					RMS (m)	0.088	0.125
50 XY	**Residual (m)**	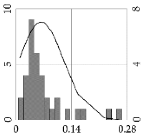	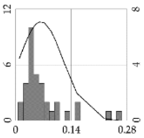	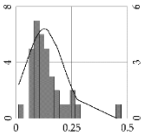	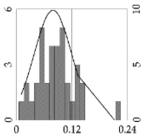	**Min**	0.001
						Max	0.125
						StdDev	0.036
						Mean	0.046
						RMS (m)	0.058
25 XY		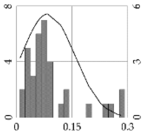	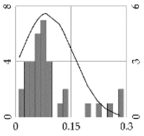	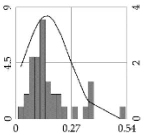	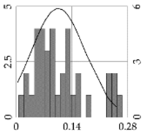	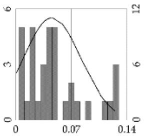	

Frequency Axis

Density Axis

Horizontal Difference Axis

Table 5. Simple multi-criteria decision making analysis scores of horizontal coordinate based analysis results.

Analysis Type	GNSS XY	TLS XY	350 XY	120 XY	50 XY	25 XY
Mean Diff. Scores	54.71	54.64	18.75	35.31	49.97	37.74
Min Diff. Scores	60.13	60.06	25.13	64.14	66.67	61.22
Max Diff. Scores	57.28	57.34	33.74	46.74	44.17	43.73
Std Dev Diff. Scores	57.56	57.62	37.96	49.89	50.60	35.08
RMS Diff. Scores	55.37	55.34	24.39	39.75	50.01	36.79
Mean Score	***57.01***	***57.00***	***27.99***	***47.17***	***52.28***	***42.91***

Point-based vertical accuracy assessment or vertical coordinate differences were examined on seven datasets by using 360 RPs. These datasets were the GNSS based vertical (Z) RP coordinates and the superimposed RPs vertical coordinates of the TLS-based minimum (TLS Min) and maximum (TLS Max) and the UAV-based raster surface models (350 Z, 120 Z, 50 Z and 25 Z). Primarily, a simple linear regression analysis was performed to compare the vertical (Z) coordinates of each dataset pair (Table 6). According to the regression analysis results, R^2 varied between 0.937 (with 71 cm root mean square deviation, RMSD) and 0.999 (with 16.83 cm RMSD). At this point, the regression analysis between the data obtained by TLS (TLS Max Z vs. TLS Min Z) was ignored (R^2 = 1.000, RMSD = 1.58 cm) because the two datasets were derived from a single data.

Table 6. Simple linear regression models of the evaluated and referenced vertical (Z) coordinate datasets and frequency-density histograms of vertical (Z) coordinates in cross-plane.

				EVALUATED				
REFERENCED **Frequency Axis**	**GNSS Z**	**TLS Max Z**	**TLS Min Z**	**350 Z**	**120 Z**	**50 Z**	**25 Z**	**Density Axis**
GNSS Z	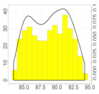	R^2 = 0.9993 Adj.R^2 = 0.9993 y = 1.0002x + 0.0837 RMSD = 0.0727	R^2 = 0.9993 Adj.R^2 = 0.9993 y = 1.0000x + 0.0985 RMSD = 0.0725	***R^2 = 0.9995*** ***Adj.R^2 = 0.9995*** ***y = 0.9985x + 0.2287*** ***RMSD = 0.0621***	***R^2 = 0.9997*** ***Adj.R^2 = 0.9997*** ***y = 1.0018x − 0.0809*** ***RMSD = 0.1683***	***R^2 = 0.9834*** ***Adj.R^2 = 0.9834*** ***y = 0.9832x + 1.6381*** ***RMSD = 0.3626***	***R^2 = 0.9382*** ***Adj.R^2 = 0.9381*** ***y = 0.9652x + 3.3146*** ***RMSD = 0.7031***	
TLS Max Z	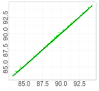	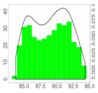	R^2 = 1.0000 Adj.R^2 = 1.0000 y = 0.9997x + 0.0163 RMSD = 0.0158	***R^2 = 0.9993*** ***Adj.R^2 = 0.9993*** ***y = 0.9978x + 0.1837*** ***RMSD = 0.0748***	***R^2 = 0.9996*** ***Adj.R^2 = 0.9996*** ***y = 1.0012x − 0.1305*** ***RMSD = 0.2691***	***R^2 = 0.9842*** ***Adj.R^2 = 0.9841*** ***y = 0.9830x + 1.5512*** ***RMSD = 0.3544***	***R^2 = 0.9398*** ***Adj.R^2 = 0.9396*** ***y = 0.9655x + 3.1907*** ***RMSD = 0.6942***	
TLS Min Z	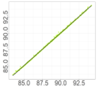	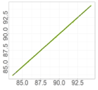	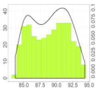	***R^2 = 0.9993*** ***Adj.R^2 = 0.9993*** ***y= 0.9981x + 0.1693*** ***RMSD = 0.0753***	***R^2 = 0.9996*** ***Adj.R^2 = 0.9996*** ***y = 1.0014x − 0.1457*** ***RMSD = 0.2925***	***R^2 = 0.9844*** ***Adj.R^2 = 0.9844*** ***y = 0.9834x + 1.5248*** ***RMSD = 0.3514***	***R^2 = 0.9403*** ***Adj.R^2 = 0.9401*** ***y = 0.9660x + 3.1531*** ***RMSD = 0.6913***	
350 Z	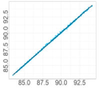	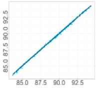	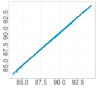	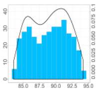	R^2 = 0.9997 Adj.R^2 = 0.9997 y = 1.0030x − 0.2879 RMSD = 0.5744	R^2 = 0.9827 Adj.R^2 = 0.9827 y = 0.9841x + 1.4652 RMSD = 0.3703	R^2 = 0.9370 Adj.R^2 = 0.9369 y = 0.9658x + 3.1698 RMSD = 0.7100	
120 Z	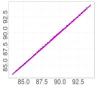	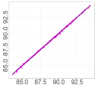	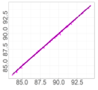	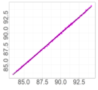	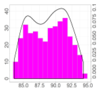	R^2 = 0.9838 Adj.R^2 = 0.9838 y = 0.9815x + 1.7111 RMSD = 0.3581	R^2 = 0.9389 Adj.R^2 = 0.9387 y = 0.9637x + 3.3746 RMSD = 0.6994	
50 Z	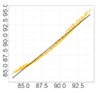	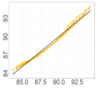	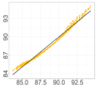	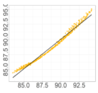	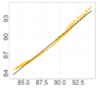	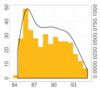	R^2 = 0.9851 Adj.R^2 = 0.9850 y = 0.9975x + 0.2989 RMSD = 0.3456	
25 Z	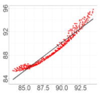	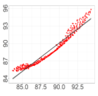	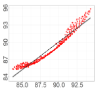	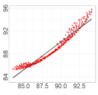	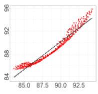	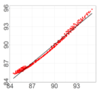	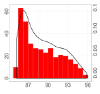	
				Z Values				

To determine the point-based vertical differences between the datasets, the minimum, maximum, standard deviation, median, NMAD and RMS values in each pair of datasets were calculated from the actual and absolute differences (Table 7). In addition, distributions of the residuals were tested via visual methods (Q-Q plots and histograms) (Figure S1).

A close examination of the vertical difference values shows that the results were quite different from the situation of the horizontal coordinate differences. According to the results of the vertical difference analysis performed with reference to the GNSS-acquired vertical coordinates, the best results were obtained by the 120-m AGL flight with 7.9 cm mean, 7.9 cm absolute and 9.3 cm RMS difference values. In addition, when the entire vertical difference results were examined (Table 7), "TLS min" had the best comparison results, where the mean of the mean absolute differences was 17.9 cm, and the mean of the RMS differences was 22.3 cm. After this result, we obtained the difference comparison results (mean of the mean absolute differences and mean of the RMS differences) of the 120-m AGL flight (18 cm and 22.6 cm), TLS max (18.2 cm and 22.6 cm), 350-m AGL flight (19.2 cm and 23.7 cm), GNSS (21.2 cm and 26.6 cm), 50-m AGL flight (30 cm and 36.8 cm) and 25-m AGL flight (53.8 cm and 66.1 cm).

To find the most reliable dataset according to the results of the vertical-coordinate-based analysis, the vertical mean absolute difference (Mean A. Diff.), vertical minimum absolute difference (Min A. Diff.), vertical maximum absolute difference (Max A. Diff.), standard deviation of vertical absolute differences (Std. Dev. A. Diff.), vertical RMS difference (RMS Diff.), median, NMAD and regression analysis results (R^2 and RMSD) were evaluated by the multi-criteria decision-making analysis. According to the vertical simple multi-criteria decision-making analysis scores, GNSS Z was the most reliable vertical dataset; among the UAV-based data, the highest score was achieved by 350 Z (Table 8).

Table 7. Vertical (Z) coordinate difference results.

REFERENCED		EVALUATED											
		TLS Max Z		**TLS Min Z**		**350 Z**		**120 Z**		**50 Z**		**25 Z**	
		Diff. (m)	**A. Diff. (m)**	**Diff. (m)**	**A. Diff. (m)**	**Diff. (m)**	**A. Diff. (m)**	**Diff. (m)**	**A. Diff. (m)**	**Diff. (m)**	**A. Diff. (m)**	**Diff. (m)**	**A. Diff. (m)**
GNSS Z	**Min**	−0.016	0.011	−0.027	0.004	***−0.113***	***0.000***	***−0.028***	***0.000***	***−0.345***	***0.000***	***−0.666***	***0.001***
	Max	0.523	0.523	0.521	0.521	***0.351***	***0.351***	***0.269***	***0.269***	***1.097***	***1.097***	***2.045***	***2.045***
	Std Dev	0.073	0.073	0.072	0.072	***0.062***	***0.059***	***0.048***	***0.047***	***0.366***	***0.250***	***0.710***	***0.456***
	Mean	0.105	0.105	0.096	0.096	***0.097***	***0.099***	***0.079***	***0.079***	***0.145***	***0.304***	***0.224***	***0.589***
	Median	0.085	0.085	0.076	0.076	***0.089***	***0.089***	***0.068***	***0.068***	***0.048***	***0.230***	***0.036***	***0.481***
	NMAD	0.041		0.040		***0.043***		***0.039***		***0.377***		***0.733***	
	RMS	0.128		0.120		***0.115***		***0.093***		***0.394***		***0.744***	
TLS Max Z	**Min**			−0.163	0.000	***−0.366***	***0.000***	***−0.408***	***0.000***	***−0.492***	***0.001***	***−0.763***	***0.002***
	Max			0.000	0.163	***0.200***	***0.366***	***0.123***	***0.408***	***0.876***	***0.876***	***1.818***	***1.818***
	Std Dev			0.016	0.016	***0.075***	***0.054***	***0.056***	***0.049***	***0.358***	***0.199***	***0.701***	***0.405***
	Mean			−0.009	0.009	***−0.008***	***0.053***	***−0.026***	***0.038***	***0.040***	***0.300***	***0.119***	***0.585***
	Median			−0.004	0.004	***0.002***	***0.037***	***−0.015***	***0.022***	***−0.045***	***0.293***	***−0.048***	***0.549***
	NMAD			0.006		***0.055***		***0.031***		***0.401***		***0.783***	
	RMS			0.018		***0.075***		***0.062***		***0.360***		***0.711***	
TLS Min Z	**Min**					***−0.365***	***0.000***	***−0.407***	***0.000***	***−0.475***	***0.001***	***−0.738***	***0.000***
	Max					***0.200***	***0.365***	***0.132***	***0.407***	***0.876***	***0.876***	***1.819***	***1.819***
	Std Dev					***0.076***	***0.052***	***0.056***	***0.047***	***0.355***	***0.201***	***0.698***	***0.407***
	Mean					***0.001***	***0.054***	***−0.017***	***0.035***	***0.049***	***0.296***	***0.128***	***0.582***
	Median					***0.014***	***0.039***	***−0.006***	***0.020***	***−0.034***	***0.289***	***−0.042***	***0.549***
	NMAD					***0.054***		***0.030***		***0.393***		***0.774***	
	RMS					***0.076***		***0.059***		***0.358***		***0.710***	
350 Z	**Min**							−0.230	0.000	−0.528	0.001	−0.857	0.002
	Max							0.201	0.230	0.998	0.998	1.946	1.946
	Std Dev							0.050	0.036	0.373	0.211	0.717	0.416
	Mean							−0.018	0.039	0.049	0.311	0.127	0.597
	Median							−0.020	0.031	−0.052	0.286	−0.067	0.545
	NMAD							0.037		0.394		0.754	
	RMS							0.053		0.376		0.728	
120 Z	**Min**									−0.417	0.001	−0.753	0.000
	Max									0.989	0.989	1.937	1.937
	Std Dev									0.362	0.211	0.707	0.418
	Mean									0.066	0.301	0.145	0.588
	Median									−0.027	0.271	−0.039	0.520
	NMAD									0.386		0.364	
	RMS									0.368		0.722	
50 Z	**Min**											−0.398	0.000
	Max											0.948	0.948
	Std Dev											0.346	0.208
	Mean											0.078	0.287
	Median											−0.008	0.252
	NMAD											0.364	
	RMS											0.354	

Table 8. Simple multi-criteria decision making analysis scores of vertical coordinate based analysis results.

Analysis Type	GNSS Z	TLS Max Z	TLS Min Z	350 Z	120 Z	50 Z	25 Z
R^2 Scores	78.68	78.68	79.42	79.47	78.39	74.50	15.16
RMSD Scores	67.67	66.72	66.29	57.45	45.57	50.84	10.00
Mean A. Diff. Scores	65.48	70.65	71.13	68.85	70.89	50.53	10.10
Min A. Diff. Scores	74.49	79.11	91.04	93.08	97.86	93.84	92.57
Max A. Diff. Scores	66.09	71.86	71.90	70.94	71.09	57.43	15.55
Std Dev A. Diff. Scores	67.36	73.50	73.50	72.22	72.97	55.16	16.18
RMS Diff. Scores	65.92	71.42	71.74	69.84	71.38	51.79	11.43
Median	86.18	40.27	43.51	39.31	38.82	30.33	24.98
NMAD	73.44	72.49	72.92	72.05	73.51	51.08	11.63
Mean Score	***71.70***	***69.41***	***71.27***	***69.25***	***68.94***	***57.28***	***23.07***

3.2.2. Areal and Volumetric Analysis

The areal and volumetric difference analyses were performed on the TLS-based minimum (TLS Min) and maximum (TLS Max) raster surface models and UAV-based 350-, 120-, 50- and 25-m flight

DSMs. In this context, the false positive (F.P.), false negative (F.N) and no difference zones were determined for each pair of datasets. The total (T. Diff.) and absolute total (A.T. Diff.) areal and volumetric differences were also calculated (Table 9 and Figure 6).

Table 9. Volumetric and areal differences for each DSM pair.

REFERENCED		EVALUATED									
		TLS Min Z		**350 Z**		**120 Z**		**50 Z**		**25 Z**	
		Volume (m^3)	**Area (m^2)**	**Volume (m^3)**	**Area (m^2)**	**Volume (m^3)**	**Area (m^2)**	**Volume (m^3)**	**Area (m^2)**	**Volume (m^3)**	**Area (m^2)**
TLS Max Z	*F.P.*	0.000	0.000	168.763	3245.343	***30.530***	***1732.374***	***1159.574***	***3149.960***	***2401.601***	***3257.313***
	F.N.	58.359	5178.640	225.280	3320.448	***247.318***	***4833.053***	***807.084***	***3416.043***	***1420.857***	***3308.710***
	T. Diff.	−58.359	5178.640	−56.518	75.105	***−216.788***	***3100.679***	***352.491***	***266.083***	***980.743***	***51.397***
	A.T. Diff.	58.359	5178.640	394.043	6565.791	***277.848***	***6565.428***	***1966.658***	***6566.003***	***3822.458***	***6566.023***
	No Diff. Area (m^2)		1387.970	0.712		***0.587***		***0.053***		***0.025***	
	A.T. Diff. V/A		0.011	0.060		***0.042***		***0.300***		***0.582***	
TLS Min Z	*F.P.*			196.805	3719.098	***46.800***	***2380.819***	***1182.040***	***3217.421***	***2424.525***	***3294.550***
	F.N.			194.846	2847.013	***205.061***	***4184.533***	***771.108***	***3348.571***	***1385.424***	***3271.469***
	T. Diff.			1.959	872.085	***−158.261***	***1803.714***	***410.932***	***131.150***	***1039.101***	***23.081***
	A.T. Diff.			391.651	6566.112	***251.861***	***6565.352***	***1953.149***	***6565.992***	***3809.949***	***6566.019***
	No Diff. Area (m^2)				0.391	***0.662***		***0.064***		***0.028***	
	A.T. Diff. V/A				0.060	***0.038***		***0.297***		***0.580***	
350 Z	*F.P.*					***65.779***	***1923.091***	***1229.582***	***3181.161***	***2471.911***	***3270.461***
	F.N.					***225.750***	***4637.043***	***821.065***	***3382.532***	***1435.583***	***3295.330***
	T. Diff.					***−159.972***	***2713.952***	***408.518***	***201.371***	***1036.327***	***24.869***
	A.T. Diff.					***291.529***	***6560.134***	***2050.647***	***6563.692***	***3907.494***	***6565.791***
	No Diff. Area (m^2)						***0.534***	***0.142***		***0.036***	
	A.T. Diff. V/A						***0.044***	***0.312***		***0.595***	
120 Z	*F.P.*							1263.954	3306.675	2510.298	3340.528
	F.N.							694.730	3257.542	1313.198	3224.757
	T. Diff.							569.224	49.134	1197.101	115.771
	A.T. Diff.							1958.684	6564.217	3823.496	6565.286
	No Diff. Area (m^2)								0.047	0.009	
	A.T. Diff. V/A								0.298	0.582	
50 Z	*F.P.*									1248.394	3377.674
	F.N.									620.406	3187.482
	T. Diff.									627.988	190.192
	A.T. Diff.									1868.799	6565.156
	No Diff. Area (m^2)										0.036
	A.T. Diff. V/A										0.285

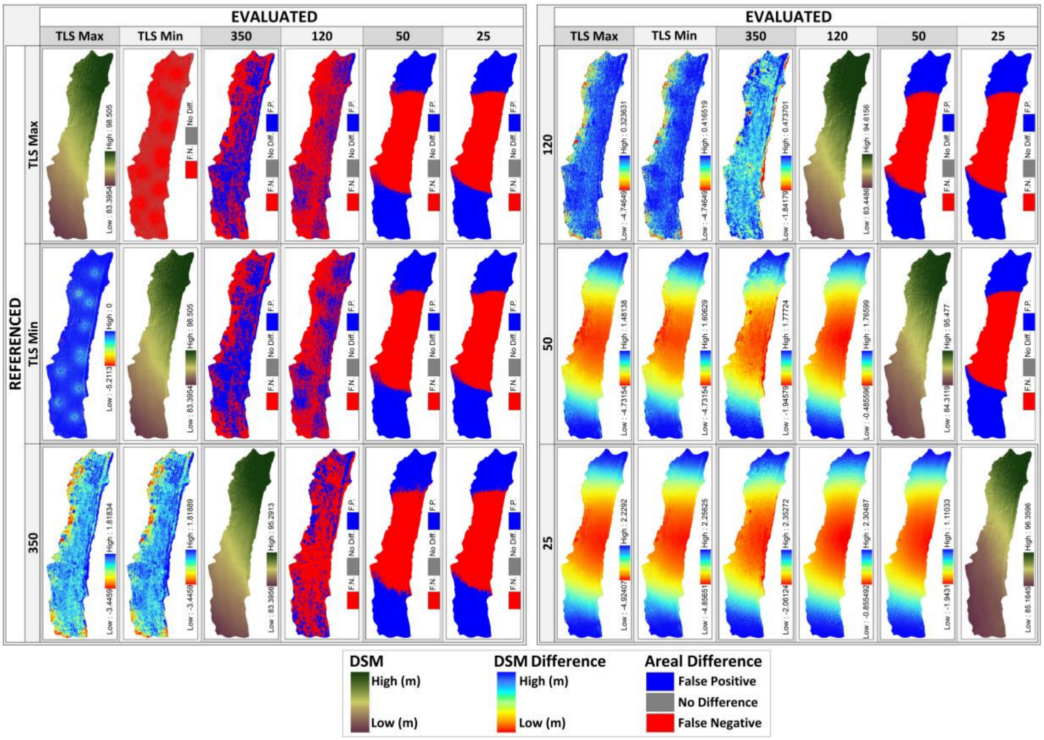

Figure 6. Clipped DSMs, DSM differences and difference zones of DSM pairs.

When the analysis results were interpreted, the minimum volumetric and areal differences were predictably obtained with the TLS Max Z–TLS Min Z comparison. However, the maximum volumetric difference was obtained with the 350 Z–25 Z comparison. Although the maximum areal difference was obtained with the TLS Min Z–350 Z comparison, the volumetric difference of this comparison was the fifth best result. To eliminate this contradiction and more objectively interpret the comparison results, the difference volume per square meter (A.T. Diff. V/A) was calculated for each pair of datasets using the absolute total volumetric and absolute total areal difference values.

In this context, to find the most reliable dataset, all areal and volumetric difference metrics were evaluated by the multi-criteria decision-making analysis (Table 10). According to analysis results, TLS Min was the most reliable vertical dataset compared to other datasets. According to the analysis results, TLS Min was the most reliable vertical dataset. Among the UAV-based data, the 120 Z and 350 Z scores were almost identical (43.75 and 43.64, respectively).

Table 10. Simple multi-criteria decision making analysis scores of areal and volumetric analysis results.

Analysis Type	TLS Max Z	TLS Min Z	350 Z	120 Z	50 Z	25 Z
F.P. Vol. Scores	70.04	69.33	67.07	68.79	51.53	11.91
F.N. Vol. Scores	64.17	66.27	62.09	65.23	50.30	14.56
A.T. Diff. Vol. Scores	67.64	67.92	64.96	67.20	50.61	11.98
F.P. Area Scores	38.78	32.18	17.51	31.79	12.71	11.05
F.N. Area Scores	50.06	60.58	72.15	49.38	79.78	82.39
A.T. Diff. Area Scores	20.02	20.01	0.13	0.15	0.08	0.03
No Diff. Area Scores	20.02	20.02	0.03	0.03	0.00	0.00
A.T. Diff. V/A Scores	67.84	68.12	65.22	67.47	50.81	12.03
Mean Score	***49.82***	***50.55***	***43.64***	***43.75***	***36.98***	***17.99***

3.3. Experimental Doming Modeling

According to all vertical data comparison results, the most unreliable vertical datasets were the 25-m and 50-m AGL surface models. When the entire vertical evaluation results were assessed, it is striking that 25-m and 50-m AGL altitude surface model datasets were extremely warped along the study area. This warping effect is expressed as "doming" in the literature [33,35–37] and can be more clearly observed in datasets with the vertical profile analysis (Figure 7).

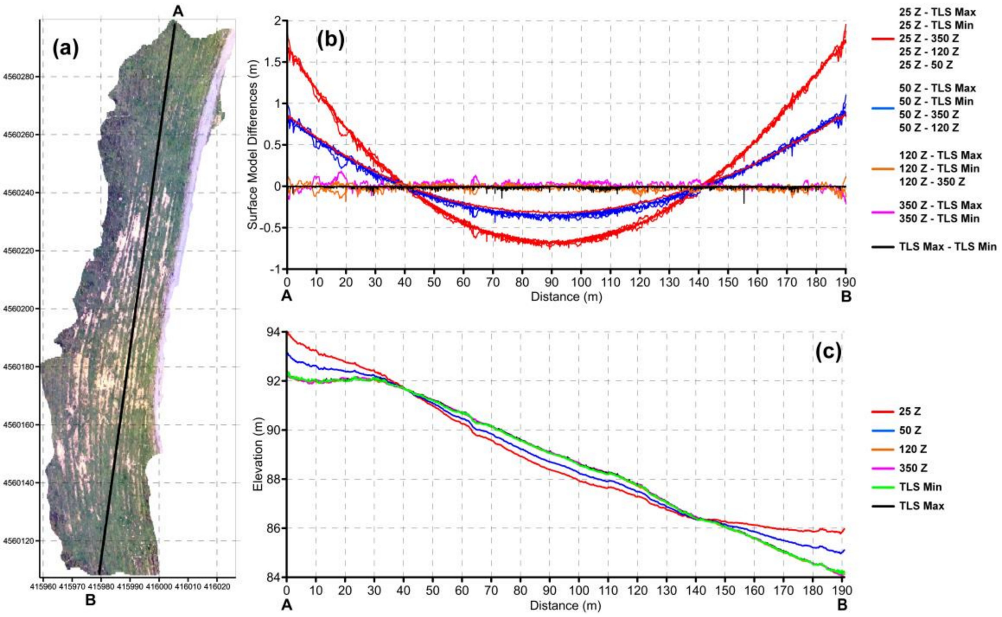

Figure 7. Comparison of surface model differences (**b**) and surface model elevations (**c**) along the same profile line A–B (**a**).

To define the "doming effect", domes were mathematically modeled as surface functions and spheres. In this context, spherical dome models were generated from the quadratic and cubic surface functions of the GNSS Z–50 Z and GNSS Z–25 Z differences. The spatial conformity of the spherical dome models and the quadratic and cubic surface functions with the actual residuals was tested, and the mean and standard deviation of distances were calculated (Figure S2 and Table 11).

Table 11. Spatial parameters of fitted functional and spherical surfaces.

	Quadratic Functions		**Cubic Functions**	
	GNSS Z–50 Z	**GNSS Z–25 Z**	**GNSS Z–50 Z**	**GNSS Z–25 Z**
Mean Distance of actual residuals from fitted surfaces (m)	−0.0003	−0.0006	−0.0002	−0.0003
Std. Dev. of distances from fitted surfaces (m)	0.042	0.060	0.040	0.048
Radius of Spherical Dome Model (m)	3478.919	1839.072	3452.649	1831.117
Mean Distance of actual residuals from fitted spheres (m)	0.066	0.064	0.081	0.075
Std. Dev. of distances from fitted spheres (m)	0.048	0.055	0.053	0.059

According to the results, an approximately 1.9-fold difference was obtained between the fitted sphere radii of GNSS Z–50 Z and GNSS Z–25 Z. In addition, cubic surface functions had better results than the other surface fitting models. To verify the results, the functional and spherical surfaces were used to remove the "doming" from the 25- and 50-m DSMs. In this context, 25- and 50-m DSMs were regenerated by using quadratic, cubic, quadratic-based spherical and cubic-based spherical surfaces. Subsequently, the surface model differences of the regenerated 25- and 50-m DSMs from TLS-Max, TLS-Min, 350- and 120-m DSMs were recalculated. According to the vertical profile analysis results of the difference surfaces, the quadratic and spherical models delivered some deformations (Figure 8). The results indicate that cubic surface functions are the best tools to model the "doming effect".

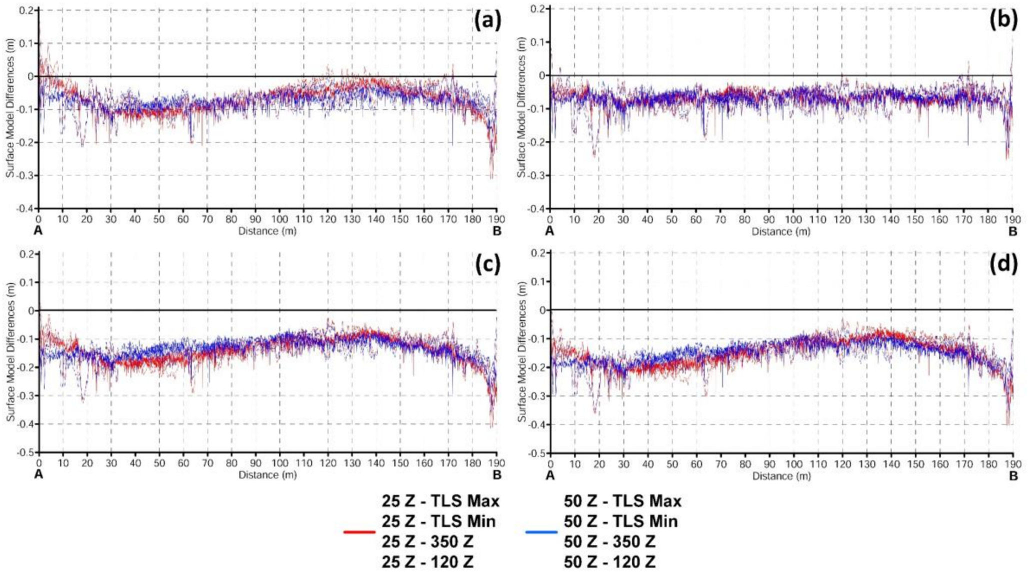

Figure 8. Differences of regenerated 25 Z and 50 Z surface models from other surface models along the profile line A-B in Figure 7. Regenerated 25 Z and 50 Z surface models derived from: quadratic surface functions (**a**); cubic surface functions (**b**); quadratic function based spherical surfaces (**c**); and cubic function based spherical surfaces (**d**).

4. Discussion

Each equipment or technique has its own methodological procedures, options, specifications, data characteristics and accuracies. An accuracy assessment should be performed, especially if the findings are to be used as an input in the decision-making process [3,66]. In addition, to find the effect of a specific factor on the accuracy, first, all possible sources of errors should be kept constant in an experimental environment. In this context, according to results, the UAV-SfM surveying workflow-derived data production has some key points. The spatial accuracy of the UAV-SfM-derived data is substantially based on the GNSS data accuracy. Two types of GNSS inputs are used in photogrammetric processes: GCP coordinates and image coordinates. In this study, the GCP coordinates were collected with the dual-frequency (L1+L2) NRTK GNSS receiver. The image coordinates were synchronously collected to the image acquisitions with the on-UAV GNSS receivers. Both UAV platform (DJI Phantom 3 Adv. and Trimble UX5) have single-frequency (L1) GNSS receivers and no RTK capabilities. As known, the dual-frequency NRTK GNSS receivers acquire more accurate location information than the single-frequency GNSS receivers [14]. Thus, this information should be considered when determining the precision thresholds in photogrammetric processes.

Another point to consider is the photogrammetry software to use in the study. Although the performance of different SfM-based software packages is discussed in the literature [67,68], the development of better image-matching algorithms and techniques is an ongoing research topic [21,69,70].

Increasing the resolution or point density is one of the factors that affects the cost of the data acquisition, and generating accurate information from low-resolution data is a challenge. In this study, five different ortho imagery datasets (25-, 50-, 120-, and 350-m AGL flights and intensity-based TLS) were generated, and the results indicate that increasing the resolution of the UAV imagery does not always lead to more accurate results, as similarly reported by Gómez-Candón, et al. [71].

The selection of appropriate techniques to use in the accuracy assessment of the third-dimension data requires an additional evaluation. By nature, PC datasets show an irregular point distribution on the surface. Although different techniques can be used in comparing the PC datasets with one another, such as the iterative closest point (ICP) algorithm, the irregular distribution of points can be considered a difficulty. At this point, it is obviously easier to compare the datasets by transforming the irregularly spaced PC data into a regular spaced grid (raster) structure. However, an interpolation technique must be used to perform this transformation. The selection of an appropriate interpolation technique to obtain raster-based surface model datasets from PCs is another factor to consider. When the literature is examined, some interpolation techniques are widely studied [49,57,72]. However, as stated by Kim, et al. [73], using an interpolation routine can result in over-smoothed raster surface models. In this context, it is appropriate to create a raster surface model from the ultra-high density PCs with at least one point in each raster grid cell. Accordingly, in this study, the raster-based surface model datasets were generated from photogrammetric and TLS-based PCs using the IDW interpolation combined binning approach. The accuracy assessment of the surface models was performed based on the point-based coordinate, areal, volumetric differences. All assessment results show that similarly to the 2D assessments, increasing the resolution does not always lead to more accurate results. In particular, the low-altitude data (25- and 50-m AGL flights) were affected by the phenomenon called the “doming effect”, which is considered an imperfection of the 3D reconstruction algorithm for photogrammetric processes. In addition, according to the results, the “doming effect” increased by 1.9-fold and was inversely proportional to the increase from 25 to 50 m AGL flight altitudes. These two datasets were generated using the DJI Phantom 3 Adv. UAV system. The 120-m AGL data acquisitions were also performed using the DJI Phantom 3 Adv. UAV system. However, the 120-m AGL DSM was obtained as doming-free. Among these three data acquisition procedures, only the AGL flight altitudes were changed, whereas the computational parameters were identical. Due to the differences in flight altitudes, the GSD of photos and number of photos varied. To define the doming effect, the deformation of the difference surfaces was modeled as quadratic and cubic surface functions. The quadratic- and cubic-based fitted spherical surfaces were also modeled. Magri and Toldo [38] demonstrated that the quadratic surface functions derived from the bare earth surface model can be used to model the "doming effect". Differently, in this study, the "doming effect" was modeled via the vertical coordinate differences of RPs from doming-affected DSMs. The findings of the current study indicate that the cubic surface functions had better results than the quadratic surface functions. In this context, three possible scenarios can be set up to generate doming-free DSMs, such as increasing the number of checkpoints to model the cubic function of the dome by using the check point coordinates and domed surface differences. The other less intensive solution is to derive the cubic function of the dome by using the differences between a doming-free surface and a domed surface. According to results for this study area, doming-free surfaces were generated at minimum 120 m AGL flight altitude. The differences between the two datasets can be determined by systematically employed points and be used as a base to model the cubic dome function. Subsequently, by applying the cubic function-derived surface model to the domed DSM, doming-free DSM can be achieved.

5. Conclusions

This study was conducted to investigate the effects of different altitudes, platforms and camera combinations on the UAV-SfM based data accuracy and "doming effect". The time spent performing the study and the accuracy of the data are the most important factors affecting the cost. This study demonstrated that it is possible to use the low-cost UAVs for mapping purposes in appropriate conditions.

According to the vertical and horizontal accuracy and multi-criteria decision-making analysis, the 120-m AGL flight provided the most reasonable accuracy for the low-cost UAV system with the mean multi-criteria decision-making analysis score of 53.29. For the mapping purpose UAV system (350-m AGL flight), the score was 46.96. When these datasets were compared with the data obtained using ground-based measurement methods, satisfactory results were obtained. As indicated in study, systematic "doming effect" was determined in the processed data of low-altitude flights (50 and 25 m AGL). This problem is generally manifested by extreme GCP-RMSE values in photogrammetric processes. In this study, total GCP-RMSEs were obtained as 0.28 and 0.55 m for 50 and 25 m AGL flights, respectively. The change in GCP-RMSEs for these datasets was about twofold. According to the vertical and volumetric difference and fitted surface analysis results, the difference ratio of "doming effect" increased by 1.9-fold and was inversely proportional to the increase from 25 to 50 m AGL flight altitudes. In this context, it was concluded that decreasing the distance between the surface and the sensor increases the "doming effect" on the data. The analysis also showed that the "doming effect" can be modeled by using cubic surface functions. One of the major findings of this study is that the "doming effect" can be effectively mitigated by applying these functional surfaces over the domed DSMs.

SfM-based photogrammetric 3D data production has several drawbacks, and those are mostly based on the use of optical imagery. In this context, the photogrammetry-based disadvantages can be substantially eliminated by post-processing procedures based on referenced data. Another approach that can be suggested to completely eliminate the disadvantages of the photogrammetry, is the laser scanning assisted image acquisition. However, the higher cost of the laser scanners and integrated high-precision navigational components (IMU and GNSS) limits the widespread usage of this technique. The UAV-SfM combination provides relatively acceptable results and cost-effective data in obtaining DSM and ortho-images when the conditions set forth in this study are taken into account. It should also be noted that, if the case is to obtain the digital terrain model, the UAV-SfM combination is employed only in bare ground terrain or very low vegetation covered areas.

Supplementary Materials: The following are available online at http://www.mdpi.com/2220-9964/8/4/175/s1, Figure S1: Q-Q plots and histograms of vertical residuals. Figure S2: Quadratic and Cubic surface functions and parameters, Quadratic and Cubic surface function-based spherical dome model parameters, the mean and standard deviation of difference distances of the generated models from the actual residual points.

Funding: This research was supported by the Istanbul University—Cerrahpasa Scientific Research Projects Coordination Department with the grant number FBA-2016-3743. This paper received no external funding for APC.

Acknowledgments: I would like to thank Mustafa Akgul, Serhat Mercan, Alican Dogru, Atakan Canbay and Hayrettin Demirci for their valuable assistance in the field. In addition, I thank the editor and the anonymous reviewers for their constructive comments that helped to improve the manuscript.

Conflicts of Interest: The author declares no conflict of interest. The funders had no role in the design of the study; in the collection, analyses, or interpretation of data; in the writing of the manuscript, or in the decision to publish the results.

References

1. Ghilani, C.D.; Wolf, P.R. *Elementary Surveying: An Introduction to Geomatics*, 13th ed.; Pearson Education: Upper Saddle River, NJ, USA, 2011.
2. Li, Z.; Zhu, Q.; Gold, C. *Digital Terrain Modeling: Principles and Methodology*; CRC Press: New York, NY, USA, 2005; p. xvi. 323p.
3. Lillesand, T.; Kiefer, R.W.; Chipman, J. *Remote Sensing and Image Interpretation*, 7th ed.; Wiley: Hoboken, NJ, USA, 2014.
4. Ouédraogo, M.M.; Degré, A.; Debouche, C.; Lisein, J. The evaluation of unmanned aerial system-based photogrammetry and terrestrial laser scanning to generate DEMs of agricultural watersheds. *Geomorphology* **2014**, *214*, 339–355. [CrossRef]
5. Jaakkola, A.; Hyyppä, J.; Kukko, A.; Yu, X.; Kaartinen, H.; Lehtomäki, M.; Lin, Y. A low-cost multi-sensoral mobile mapping system and its feasibility for tree measurements. *ISPRS J. Photogramm. Remote Sens.* **2010**, *65*, 514–522. [CrossRef]
6. Mechelke, K.; Kersten, T.P.; Lindstaedt, M. Comparative investigations into the accuracy behaviour of the new generation of terrestrial laser scanning systems. In Proceedings of the 8th Conference on Optical 3-D Measurement Techniques, Zürich, Germany, 9–12 July 2007; pp. 319–327.
7. Kersten, T.P.; Mechelke, K.; Lindstaedt, M.; Sternberg, H. Methods for Geometric Accuracy Investigations of Terrestrial Laser Scanning Systems. *Photogramm. Fernerkund. Geoinf.* **2009**, *2009*, 301–315. [CrossRef]
8. Sanz-Ablanedo, E.; Chandler, J.H.; Rodríguez-Pérez, J.R.; Ordóñez, C. Accuracy of Unmanned Aerial Vehicle (UAV) and SfM Photogrammetry Survey as a Function of the Number and Location of Ground Control Points Used. *Remote Sens.* **2018**, *10*, 1606. [CrossRef]
9. Clapuyt, F.; Vanacker, V.; Van Oost, K. Reproducibility of UAV-based earth topography reconstructions based on Structure-from-Motion algorithms. *Geomorphology* **2016**, *260*, 4–15. [CrossRef]
10. Yang, G.; Li, C.; Wang, Y.; Yuan, H.; Feng, H.; Xu, B.; Yang, X. The DOM Generation and Precise Radiometric Calibration of a UAV-Mounted Miniature Snapshot Hyperspectral Imager. *Remote Sens.* **2017**, *9*, 642. [CrossRef]
11. Khaghani, M.; Skaloud, J. Autonomous Vehicle Dynamic Model-Based Navigation for Small UAVs. *J. Inst. Navig.* **2016**, *63*, 345–358. [CrossRef]
12. Vetrella, A.; Fasano, G.; Accardo, D.; Moccia, A. Differential GNSS and Vision-Based Tracking to Improve Navigation Performance in Cooperative Multi-UAV Systems. *Sensors* **2016**, *16*, 2164. [CrossRef]
13. Stöcker, C.; Nex, F.; Koeva, M.; Gerke, M. Quality assessment of combined IMU/GNSS data for direct georeferencing in the context of UAV-based mapping. *Int. Arch. Photogramm.* **2017**, *XLII-2/W6*, 355–361. [CrossRef]
14. Gerke, M.; Przybilla, H.-J. Accuracy Analysis of Photogrammetric UAV Image Blocks: Influence of Onboard RTK-GNSS and Cross Flight Patterns. *Photogramm. Fernerkund. Geoinf.* **2016**, *2016*, 17–30. [CrossRef]
15. Leitão, J.P.; De Vitry, M.M.; Scheidegger, A.; Rieckermann, J. Assessing the quality of digital elevation models obtained from mini unmanned aerial vehicles for overland flow modelling in urban areas. *Hydrol. Earth Syst. Sci.* **2016**, *20*, 1637–1653. [CrossRef]
16. Rock, G.; Ries, J.; Udelhoven, T. Sensitivity analysis of UAV-photogrammetry for creating digital elevation models (DEM). In Proceedings of the Conference on Unmanned Aerial Vehicle in Geomatics, Zurich, Switzerland, 14–16 September 2011.

17. Mesas-Carrascosa, F.-J.; Notario García, M.; Meroño de Larriva, J.; García-Ferrer, A. An Analysis of the Influence of Flight Parameters in the Generation of Unmanned Aerial Vehicle (UAV) Orthomosaicks to Survey Archaeological Areas. *Sensors* **2016**, *16*, 1838. [CrossRef]
18. Jiang, S.; Jiang, W. On-Board GNSS/IMU Assisted Feature Extraction and Matching for Oblique UAV Images. *Remote Sens.* **2017**, *9*, 813. [CrossRef]
19. Kääb, A.; Girod, L.; Berthling, I. Surface kinematics of periglacial sorted circles using structure-from-motion technology. *Cryosphere* **2014**, *8*, 1041–1056. [CrossRef]
20. Westoby, M.; Brasington, J.; Glasser, N.; Hambrey, M.; Reynolds, J. Structure-from-Motion' photogrammetry: A low-cost, effective tool for geoscience applications. *Geomorphology* **2012**, *179*, 300–314. [CrossRef]
21. Smith, M.; Carrivick, J.; Quincey, D.; Carrivick, J. Structure from motion photogrammetry in physical geography. *Prog. Phys. Geogr. Earth Environ.* **2015**, *40*, 247–275. [CrossRef]
22. Kraus, K. *Photogrammetry: Geometry from Images and Laser Scans*, 2nd ed.; Walter de Gruyter: Berlin, Germany, 2007.
23. Yan, L.; Fei, L.; Chen, C.; Ye, Z.; Zhu, R. A Multi-View Dense Image Matching Method for High-Resolution Aerial Imagery Based on a Graph Network. *Remote Sens.* **2016**, *8*, 799. [CrossRef]
24. Yanagi, H.; Chikatsu, H. Performance evaluation of 3D modeling software for UAV photogrammetry. *Int. Arch. Photogramm.* **2016**, *XLI-B5*, 147–152. [CrossRef]
25. Uysal, M.; Toprak, A.; Polat, N. DEM generation with UAV Photogrammetry and accuracy analysis in Sahitler hill. *Measurement* **2015**, *73*, 539–543. [CrossRef]
26. Polat, N.; Uysal, M. An Experimental Analysis of Digital Elevation Models Generated with Lidar Data and UAV Photogrammetry. *J. Indian Soc. Remote Sens.* **2018**, *46*, 1135–1142. [CrossRef]
27. Kršák, B.; Blišťan, P.; Pauliková, A.; Puškárová, P.; Kovanič, L'.; Palková, J.; Zelizňaková, V. Use of low-cost UAV photogrammetry to analyze the accuracy of a digital elevation model in a case study. *Measurement* **2016**, *91*, 276–287. [CrossRef]
28. Mlambo, R.; Woodhouse, I.H.; Gerard, F.; Anderson, K. Structure from Motion (SfM) photogrammetry with drone data: A low cost method for monitoring greenhouse gas emissions from forests in developing countries. *Forests* **2017**, *8*, 68. [CrossRef]
29. James, M.; Robson, S.; D'Oleire-Oltmanns, S.; Niethammer, U. Optimising UAV topographic surveys processed with structure-from-motion: Ground control quality, quantity and bundle adjustment. *Geomorphology* **2017**, *280*, 51–66. [CrossRef]
30. Wallace, L.; Lucieer, A.; Malenovský, Z.; Turner, D.; Vopěnka, P. Assessment of Forest Structure Using Two UAV Techniques: A Comparison of Airborne Laser Scanning and Structure from Motion (SfM) Point Clouds. *Forests* **2016**, *7*, 62. [CrossRef]
31. Leberl, F.; Irschara, A.; Pock, T.; Meixner, P.; Gruber, M.; Scholz, S.; Wiechert, A. Point Clouds: Lidar versus 3D Vision. *Photogramm. Eng. Remote Sens.* **2010**, *76*, 1123–1134. [CrossRef]
32. Snavely, N.; Seitz, S.M.; Szeliski, R. Modeling the world from internet photo collections. *Int. J. Comput. Vis.* **2008**, *80*, 189–210. [CrossRef]
33. James, M.R.; Robson, S. Mitigating systematic error in topographic models derived from UAV and ground-based image networks. *Earth Surf. Process. Landf.* **2014**, *39*, 1413–1420. [CrossRef]
34. Vericat, D.; Smith, M.W. From experimental plots to experimental landscapes: Topography, erosion and deposition in sub-humid badlands from Structure-from-Motion photogrammetry. *Earth Surf. Process. Landf.* **2015**, *40*, 1656–1671. [CrossRef]
35. Tonkin, T.; Midgley, N. Ground-Control Networks for Image Based Surface Reconstruction: An Investigation of Optimum Survey Designs Using UAV Derived Imagery and Structure-from-Motion Photogrammetry. *Remote Sens.* **2016**, *8*, 786. [CrossRef]
36. Wackrow, R.; Chandler, J.H. Minimising systematic error surfaces in digital elevation models using oblique convergent imagery. *Photogramm. Rec.* **2011**, *26*, 16–31. [CrossRef]
37. Wackrow, R.; Chandler, J.H. A convergent image configuration for DEM extraction that minimises the systematic effects caused by an inaccurate lens model. *Photogramm. Rec.* **2008**, *23*, 6–18. [CrossRef]
38. Magri, L.; Toldo, R. Bending the doming effect in structure from motion reconstructions through bundle adjustment. *Int. Arch. Photogramm.* **2017**, *XLII-2/W6*, 235–241. [CrossRef]
39. Turkish Directorate General of Civil Aviation. *Unmanned Aerial Systems Directive*, 2nd ed.; Ministry of Transport and Infrastructure: Ankara, Turkey, 2017; p. 35.

40. Federal Aviation Administration. *Operation and Certification of Small Unmanned Aircraft Systems*; FAA-2015-0150-4721; Department of Transportation: Washington, DC, USA, 2016; p. 152.
41. Civil Aviation Administration of China. *Civil Drone Driver Management Regulations*; AC-61-FS-2016-20R1; The State Council the People's Republic of China: Beijing, China, 2016; p. 12.
42. Civil Aviation Authority. *Air Navigation (Amendment) Order 2018—Guidance for Small Unmanned Aircraft Users*; CAP1687; United Kingdom Government: London, UK, 2018; p. 16.
43. Civil Aviation Safety Authority. *Remotely Piloted Aircraft Systems—Operation of Excluded RPA*; AC 101-10v1.3; Australian Government: Canberra, Australia, 2018; p. 32.
44. Zhou, Q.; Lees, B.; Tang, G. *Advances in Digital Terrain Analysis*; Springer: Berlin/Heidelberg, Germany, 2008.
45. Wilson, J.P.; Gallant, J.C. *Terrain Analysis: Principles and Applications*; Wiley: New York, NY, USA, 2000.
46. Wilson, J.P.; Fotheringham, A.S. *The Handbook of Geographic Information Science*; Blackwell Pub.: Malden, MA, USA, 2008.
47. Akima, H. A Method of Bivariate Interpolation and Smooth Surface Fitting for Irregularly Distributed Data Points. *ACM Trans. Math. Softw.* **1978**, *4*, 148–159. [CrossRef]
48. Hengl, T. Finding the right pixel size. *Comput. Geosci.* **2006**, *32*, 1283–1298. [CrossRef]
49. Bater, C.W.; Coops, N.C. Evaluating error associated with lidar-derived DEM interpolation. *Comput. Geosci.* **2009**, *35*, 289–300. [CrossRef]
50. Briggs, I.C. Machine contouring using minimum curvature. *Geophysics* **1974**, *39*, 39–48. [CrossRef]
51. Fortune, S. A sweepline algorithm for Voronoi diagrams. *Algorithmica* **1987**, *2*, 153–174. [CrossRef]
52. Hardy, R.L. Multiquadric equations of topography and other irregular surfaces. *J. Geophys. Res.* **1971**, *76*, 1905–1915. [CrossRef]
53. Hutchinson, M. A new procedure for gridding elevation and stream line data with automatic removal of spurious pits. *J. Hydrol.* **1989**, *106*, 211–232. [CrossRef]
54. Hutchinson, M.; Bischof, R. A new method for estimating the spatial distribution of mean seasonal and annual rainfall applied to the Hunter Valley, New South Wales. *Aust. Meteorol. Mag.* **1983**, *31*, 179–184.
55. Makarovic, B. Regressive rejection—A digital data compression technique. In Proceedings of the ASP/ACSM Fall Technical Meeting, Little Rock, AR, USA, 18–21 October 1977.
56. Makarovic, B. Structures for geo-information and their application in selective sampling for digital terrain models. *ITC J.* **1984**, *4*, 285–295.
57. Mitas, L.; Mitasova, H. Spatial interpolation. In *Geographical Information Systems: Principles, Techniques, Management and Applications*; Longley, P., Goodchild, M.F., Maguire, D.J., Rhind, D.W., Eds.; Wiley: New York, NY, USA, 1999; Volume 1, pp. 481–492.
58. Watson, D.F. *Contouring: A Guide to the Analysis and Display of Spatial Data*; Pergamon Press: Oxford, UK, 1992.
59. Zimmerman, D.; Pavlik, C.; Ruggles, A.; Armstrong, M.P. An Experimental Comparison of Ordinary and Universal Kriging and Inverse Distance Weighting. *Math. Geol.* **1999**, *31*, 375–390. [CrossRef]
60. Caruso, C.; Quarta, F. Interpolation methods comparison. *Comput. Math. Appl.* **1998**, *35*, 109–126. [CrossRef]
61. O'Sullivan, D.; Unwin, D. *Geographic Information Analysis*; Wiley: Hoboken, NJ, USA, 2010.
62. Tobler, W.R. A computer movie simulating urban growth in the Detroit region. *Econ. Geogr.* **1970**, *46*, 234–240. [CrossRef]
63. Andrew, M.; Indresan, G.; Malcolm, P.; Trevor, C. Contributions to the experimental validation of the discrete element method applied to tumbling mills. *Eng. Comput.* **2004**, *21*, 119–136. [CrossRef]
64. Powell, M.S.; McBride, A.T. What is required from DEM simulations to model breakage in mills? *Miner. Eng.* **2006**, *19*, 1013–1021. [CrossRef]
65. Höhle, J.; Höhle, M. Accuracy assessment of digital elevation models by means of robust statistical methods. *ISPRS J. Photogramm.* **2009**, *64*, 398–406. [CrossRef]
66. Senseman, G.M.; Bagley, C.F.; Tweddale, S.A. *Accuracy Assessment of the Discrete Classification of Remotely-Sensed Digital Data for Landcover Mapping*; Construction Engineering Research Laboratories (Army): Champaign, IL, USA, 1995.
67. Jaud, M.; Passot, S.; Le Bivic, R.; Delacourt, C.; Grandjean, P.; Le Dantec, N. Assessing the Accuracy of High Resolution Digital Surface Models Computed by PhotoScan® and MicMac® in Sub-Optimal Survey Conditions. *Remote Sens.* **2016**, *8*, 465. [CrossRef]
68. Barbasiewicz, A.; Widerski, T.; Daliga, K. The analysis of the accuracy of spatial models using photogrammetric software: Agisoft Photoscan and Pix4D. *E3S Web Conf.* **2018**, *26*, 12. [CrossRef]

69. Ullman, S. The interpretation of structure from motion. *Proc. R. Soc. Lond. Ser. B Biol. Sci.* **1979**, *203*, 405–426.
70. Weng, J.; Huang, T.S.; Ahuja, N. *Motion and Structure from Image Sequences*; Springer: Berlin, Germany, 1993.
71. Gómez-Candón, D.; De Castro, A.I.; López-Granados, F. Assessing the accuracy of mosaics from unmanned aerial vehicle (UAV) imagery for precision agriculture purposes in wheat. *Precis. Agric.* **2014**, *15*, 44–56. [CrossRef]
72. Guo, Q.; Li, W.; Yu, H.; Alvarez, O. Effects of topographic variability and lidar sampling density on several DEM interpolation methods. *Photogramm. Eng. Remote Sens.* **2010**, *76*, 701–712. [CrossRef]
73. Kim, S.; Rhee, S.; Kim, T. Digital Surface Model Interpolation Based on 3D Mesh Models. *Remote Sens.* **2018**, *11*, 24. [CrossRef]